

HNCO: a molecule that traces low-velocity shocks

Nai-Ping Yu, Jing-Long Xu and Jun-Jie Wang

National Astronomical Observatories, Chinese Academy of Sciences, Beijing 100012, China;
yunaiping09@mails.gucas.ac.cn
NAOC-TU Joint Center for Astrophysics, Lhasa 850000, China

Received 2017 June 30; accepted 2017 November 5

Abstract Using data from Millimetre Astronomy Legacy Team Survey at 90 GHz (MALT90), we present a molecular line study of a sample of APEX Telescope Large Area Survey of the Galaxy (ATLASGAL) clumps. Twelve emission lines have been detected in all. We found that in most sources, emissions of HC_3N , HN^{13}C , CH_3CN , HNCO and SiO show more compact distributions than those of HCO^+ , HNC, HCN and N_2H^+ . By comparing with other molecular lines, we found that the abundance of HNCO ($\chi(\text{HNCO})$) correlates well with other species such as HC_3N , HNC, C_2H , H^{13}CO^+ and N_2H^+ . Previous studies indicate the HNCO abundance could be enhanced by shocks. However, in this study, we find the abundance of HNCO does not correlate well with that of SiO, which is also a good tracer of shocks. We suggest this may be because HNCO and SiO trace different parts of shocks. Our analysis indicates that the velocity of a shock traced by HNCO tends to be lower than that traced by SiO. In the low-velocity shocks traced by HNCO, the HNCO abundance increases faster than that of SiO. While in the relatively high-velocity shocks traced by SiO, the SiO abundance increases faster than that of HNCO. We suggest that in the infrared dark cloud MSXDC G331.71+00.59, high-velocity shocks are destroying the molecule HNCO.

Key words: stars: formation — ISM: abundances — ISM: clouds — ISM: molecules

1 INTRODUCTION

The emission of interstellar isocyanic acid (HNCO) was first detected by Snyder & Buhl (1972) in Sgr B2. Since its discovery, HNCO has been found to be ubiquitous in our Galactic star-forming regions (e.g. Brown 1981; Churchwell et al. 1986; Zinchenko et al. 2000). It has also been detected in extragalactic sources and the circumstellar envelopes around asymptotic giant branch (AGB) stars (e.g. Meier & Turner 2005; Velilla Prieto et al. 2015). Observations indicate HNCO traces the densest part of molecular clouds (Jackson et al. 1984). Zinchenko et al. (2000) suggested the HNCO abundance could be enhanced by shocked gas. They found the HNCO integrated line intensities correlate well with those of SiO emissions in massive galactic dense cores, indicating a similar production mechanism of the two species. Martín et al. (2008) conducted a multitransition

study toward 13 molecular clouds in the Galactic center region. They found the $\text{HNCO}/^{13}\text{CS}$ relative abundance ratio was very sensitive to ultraviolet (UV) radiations and shocks. This abundance ratio could be used as a tool to distinguish between the influence of shocks and the radiation field in molecular clouds. Li et al. (2013) mapped nine massive star-forming regions that exhibit HNCO emissions using the Purple Mountain Observatory (PMO) 13.7 m telescope. They found possible shock enhancement of HNCO in Orion KL and W75OH, indicating shocks could enhance the HNCO abundance. They also found that the line parameters of HNCO and HC_3N have good correlations, implying similar excitation mechanisms for the two species.

Early work suggests HNCO is mainly formed through gas-phase reactions (e.g. Iglesias 1977; Turner et al. 1999). However, chemical models reveal that the abundances of HNCO derived from gas-phase reactions

are inconsistent with observations (e.g. Tideswell *et al.* 2010). To explain the observed abundances of HNC0 in star-forming regions, reactions on the surfaces of grains should be involved. In the early stage of star formation, as material collapses, a wide array of atoms and molecules is absorbed onto the dust grains. Grain-surface chemistry becomes available. Calculations indicate that this is an effective way to produce HNC0 on grain mantles (e.g. Allen & Robinson 1977; Garrod *et al.* 2008). When the gas in a region is shocked, HNC0 could be ejected into the gas-phase by low-velocity shocks (e.g. Flower *et al.* 1995; Martín *et al.* 2008). In the hot core stage of star formation, the HNC0 emissions we observe could also be formed by the destruction of more complex molecules (such as HNCHO, HNC0CHO, HNCONH and HNC0OH) after their evaporation into the gas phase (e.g. Tideswell *et al.* 2010). The destruction of HNC0 in star-forming regions is dominated by reactions with He^+ and H_3^+ (Turner *et al.* 1999). It can also be destroyed by far-UV photons and cosmic rays.

In order to investigate the physical and chemical properties of HNC0 in star-forming regions, we present a molecular line study of HNC0 in a sample of APEX Telescope Large Area Survey of the Galaxy (ATLASGAL) clumps. We introduce our data and source selections in Section 2, results in Section 3, analysis in Section 4 and summary in Section 5.

2 DATA

Our molecular line data come from Millimetre Astronomy Legacy Team Survey at 90 GHz (MALT90), which is carried out by the Mopra 22-m telescope. MALT90 is an international project aimed at characterizing the physical and chemical evolution of massive star-forming regions within our Galaxy (e.g. Foster *et al.* 2011; Jackson *et al.* 2013). Mopra is equipped with three receivers for single-dish observations. Near 90 GHz, the angular resolution of Mopra is $38''$, and the antenna efficiency ranges from 0.49 at 86 GHz to 0.42 at 115 GHz (Ladd *et al.* 2005). MALT90 maps 16 emission lines simultaneously. The velocity resolution of the data is about 0.11 km s^{-1} , with pointing accuracy $\sim 8''$, and the absolute flux uncertainty ranges from 10% to 17% depending on the transition in question (Foster *et al.* 2013). The target clumps of this survey are selected from the $870 \mu\text{m}$ sky survey of ATLASGAL (Schuller *et al.* 2009; Contreras *et al.* 2013). The data files are publicly available and can be downloaded

from the MALT90 home page¹. Using Continuum and Line Analysis Single-Disk Software (CLASS) and Grenoble Graphic (GREG) software packages, we analyzed the data. MALT90 observed more than 3000 ATLASGAL clumps. Among the 16 emission lines, HNC0 ($4_{0,4}-3_{0,3}$) is one of the least detected ones (Rathborne *et al.* 2016; Liu *et al.* 2018). In order to study HNC0, we searched for the brightest 300 ATLASGAL clumps and selected 18 sources which show distinct HNC0 emissions. Sources in the Galactic center are not included because sources in that direction always have multiple velocity components. The basic information on our sources is listed in Table 1.

Dust temperature (T_d) is essential in the study of chemical evolution in star formation regions. When T_d is below $\sim 20 \text{ K}$, carbon species like CO and CS can be depleted in cold gas. Derived from adjusting single-temperature dust emission models to the far-infrared intensity maps measured between 160 and $870 \mu\text{m}$ from the Herschel and APEX sky surveys, Guzmán *et al.* (2015) recently calculated the dust temperatures and H_2 column densities for ~ 3000 MALT90 clumps. The full width at half maximum (FWHM) of these data ranges from $12''$ to $35''$ (data from the PACS $70 \mu\text{m}$ band are excluded). To make an adequate comparison, they convolved all images to a spatial resolution of $35''$, which is the lowest resolution given by the $500 \mu\text{m}$ SPIRE instrument. We use these dust temperatures and H_2 column densities derived by Guzmán *et al.* (2015) in our study due to a similar beam resolution of Mopra ($35''$ versus $38''$). These values are also listed in Table 1. The mean dust temperature of our sample is 23.9 K . This is consistent with many other observations of massive young stellar objects (MYSOs) and HII regions (e.g., Hennemann *et al.* 2009; Sreenilayam & Fich 2011).

3 RESULTS

Among the 16 spectral lines, HCO^+ (1–0), HCN (1–0), HNC (1–0), N_2H^+ (1–0), C_2H (1–0), H^{13}CO^+ (1–0), HC_3N (10–9), HN^{13}C (1–0), HNC0 ($4_{0,4}-3_{0,3}$) and SiO (2–1) are detected in all sources, but $^{13}\text{C}^{34}\text{S}$ (2–1), HNC0 ($4_{1,3}-3_{1,2}$), HC^{13}CCN (10–9) and $\text{H}41\alpha$ are not detected in any sources.

Figure 1 to Figure 18 show the detected lines and their integrated intensities. It can be noted that emissions of HC_3N , HN^{13}C , HNC0 and SiO are more compact

¹ <http://atoa.atnf.csiro.au/MALT90>

Table 1 List of Our Sources

Source name	R.A. (J2000.0)	Dec. (J2000.0)	T_d^a (K)	$N(\text{H}_2)^a$ ($\times 10^{23} \text{ cm}^{-2}$)	Type ^a
(1)	(2)	(3)	(4)	(5)	(6)
AGAL008.671–00.356	18:06:19.13	–21:37:27.3	24.0(3.0)	3.54 (0.43)	Protostellar
AGAL008.684–00.367	18:06:23.44	–21:37:05.9	24.6(0.4)	1.15 (0.08)	Protostellar
AGAL010.472+00.027	18:08:38.18	–19:51:49.0	30.0(2.0)	5.24 (0.51)	HII
AGAL318.948–00.197	15:00:55.54	–58:58:57.5	25.6(0.4)	1.41 (0.10)	Protostellar
AGAL327.293–00.579	15:53:08.52	–54:37:06.9	28.0(1.0)	8.69 (0.62)	HII
AGAL329.029–00.206	16:00:31.95	–53:12:53.1	19.6(0.7)	2.62 (0.19)	Protostellar
AGAL329.066–00.307	16:01:09.75	–53:16:03.3	18.5(0.6)	1.07 (0.08)	Protostellar
AGAL331.709+00.582	16:10:01.56	–50:49:34.8	19.0(3.0)	1.04 (0.15)	Protostellar
AGAL331.709+00.602	16:10:01.56	–50:49:34.8	20.2(0.9)	1.09 (0.08)	Protostellar
AGAL335.586–00.291	16:30:59.08	–48:43:53.3	22.5(0.4)	2.75 (0.20)	Protostellar
AGAL337.704–00.054	16:38:29.64	–47:00:41.1	22.6(0.9)	3.08 (0.22)	HII
AGAL338.926+00.554	16:40:34.29	–45:41:41.8	20.0(1.0)	4.78 (0.34)	Protostellar
AGAL340.248–00.374	16:49:30.41	–45:17:53.6	22.0(1.0)	1.17 (0.08)	HII
AGAL345.003–00.224	17:05:11.02	–41:29:07.8	25.8(11.0)	3.38 (0.88)	Protostellar
AGAL350.111+00.089	17:19:26.61	–37:10:23.1	24.0(0.6)	1.55 (0.07)	HII
AGAL351.444+00.659	17:20:54.64	–35:45:11.8	22.0(2.0)	9.75 (0.94)	Protostellar
AGAL351.581–00.352	17:25:24.99	–36:12:45.1	24.0(1.0)	5.61 (0.40)	Protostellar
AGAL353.409–00.361	17:30:26.21	–34:41:48.9	23.0(1.0)	4.89 (0.35)	HII

Notes: ^a These values come from Guzmán et al. (2015).

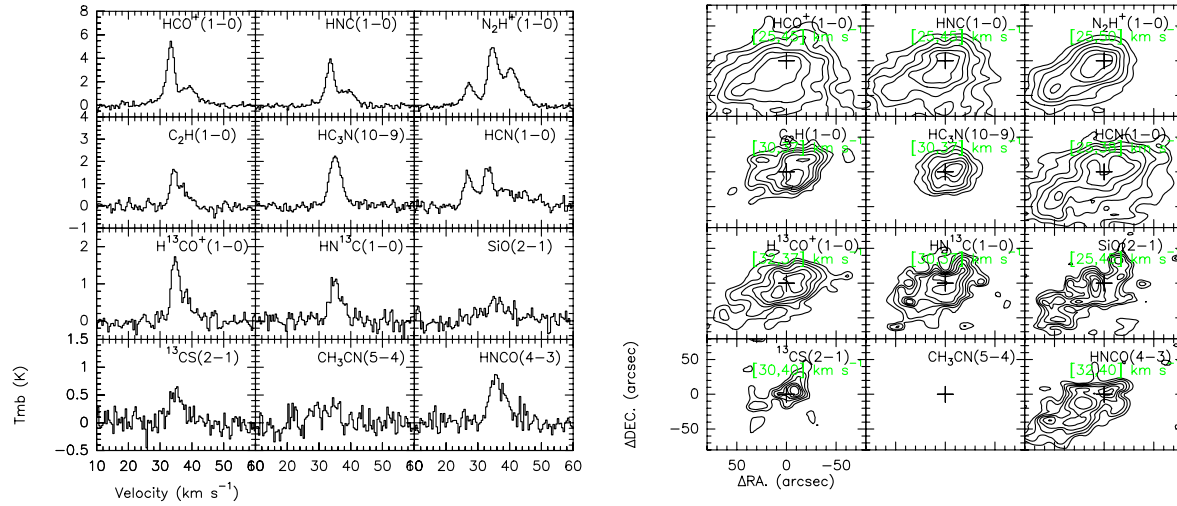


Fig. 1 Molecular spectra and integrated intensities of AGAL08.671–00.356. Contour levels are 40, 50, . . . , 90 percent of the peak emissions. The black pluses mark the 870 μm emission peaks of AGAL08.671–00.356. The green numbers show the range of integrations (Figs. 1–18 are shown in *color online*).

than those of HCO^+ , HCN , HNC and N_2H^+ in most sources. We characterize the size of a molecular cloud by using the beam deconvolved angular diameter of a circle with the same area as the half peak intensity

$$\theta(\text{species}) = 2 \left(\frac{A_{1/2}}{\pi} - \frac{\theta_{\text{beam}}^2}{4} \right)^{1/2}, \quad (1)$$

where $A_{1/2}$ is the area within the contour of half peak intensity and θ_{beam} the FWHM beam size ($38''$). The beam deconvolved angular diameters of different species are presented in Table 2.

In Figure 19, we present plots that compare beam deconvolved angular diameters of HNCO with those of other species. The sizes of HNCO clumps are comparable to those of SiO clumps.

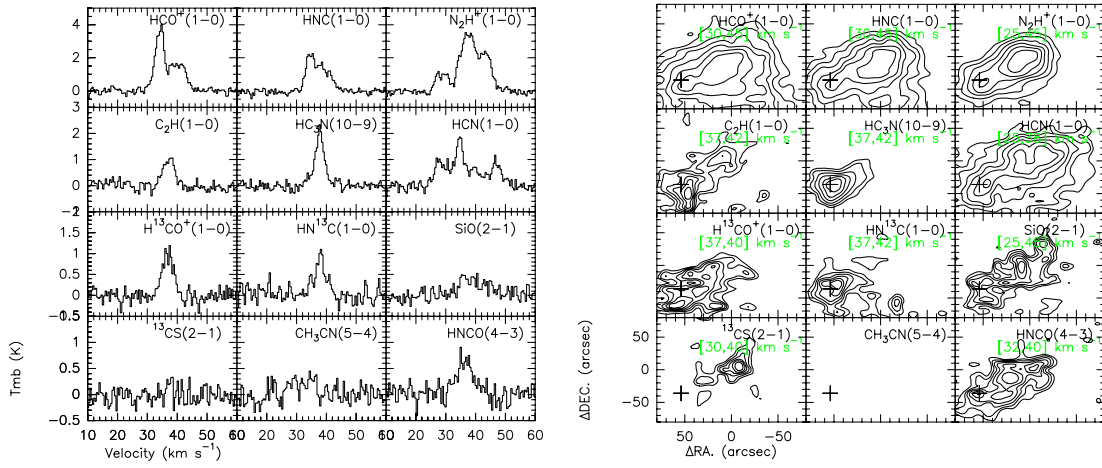


Fig. 2 Molecular spectra and integrated intensities of AGAL08.684-00.367. Contour levels are 40, 50, . . . , 90 percent of the peak emissions. The black pluses mark the 870 μm emission peaks of AGAL08.684-00.367. The green numbers show the range of integrations.

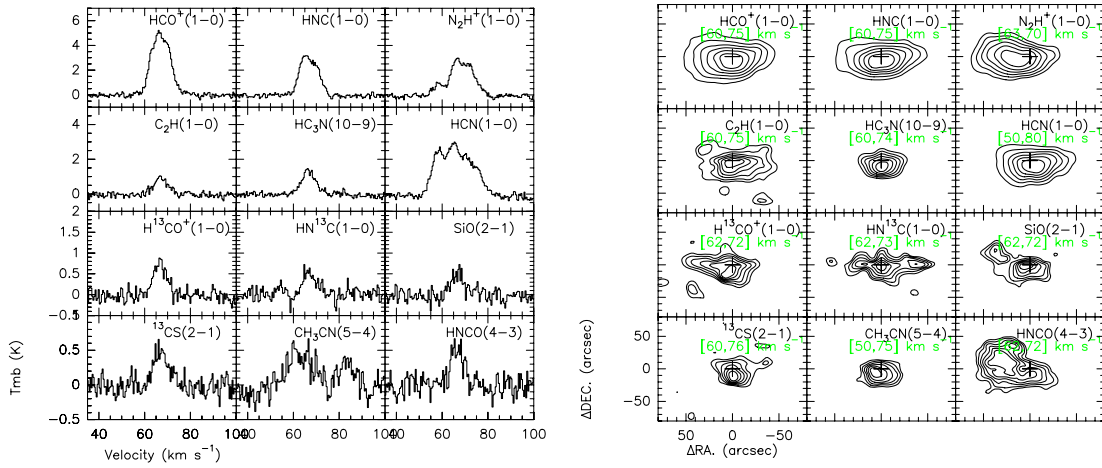


Fig. 3 Molecular spectra and integrated intensities of AGAL10.472+00.027. Contour levels are 40, 50, . . . , 90 percent of the peak emissions. The black pluses mark the 870 μm emission peaks of AGAL10.472+00.027. The green numbers show the range of integrations.

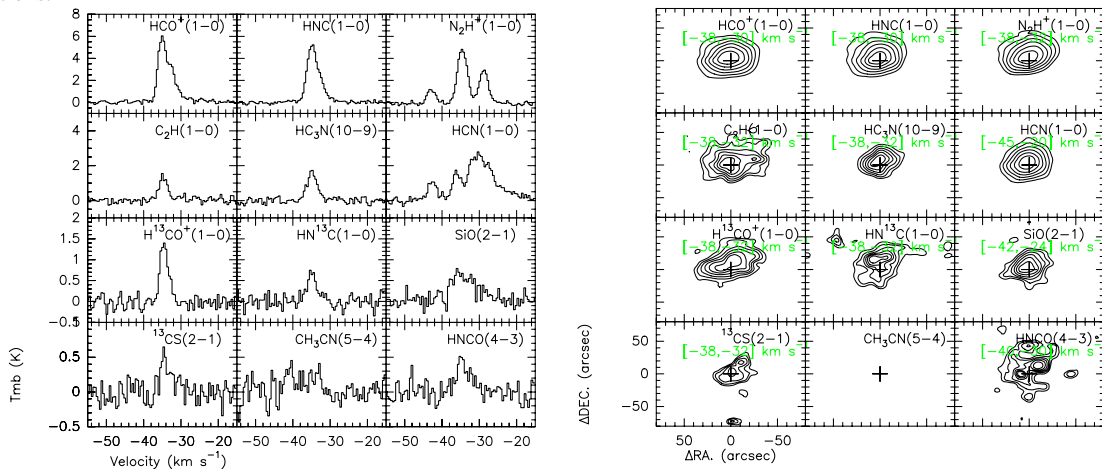


Fig. 4 Molecular spectra and integrated intensities of AGAL318.948-00.197. Contour levels are 40, 50, . . . , 90 percent of the peak emissions. The black pluses mark the 870 μm emission peaks of AGAL318.948-00.197. The green numbers show the range of integrations.

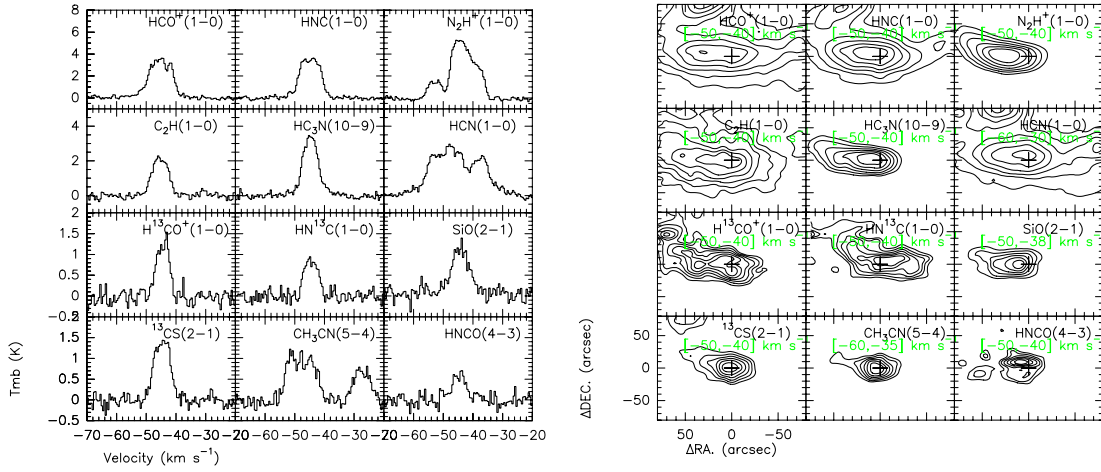


Fig. 5 Molecular spectra and integrated intensities of AGAL327.293–00.579. Contour levels are 40, 50, . . . , 90 percent of the peak emissions. The black pluses mark the 870 μm emission peaks of AGAL327.293–00.579. The green numbers show the range of integrations.

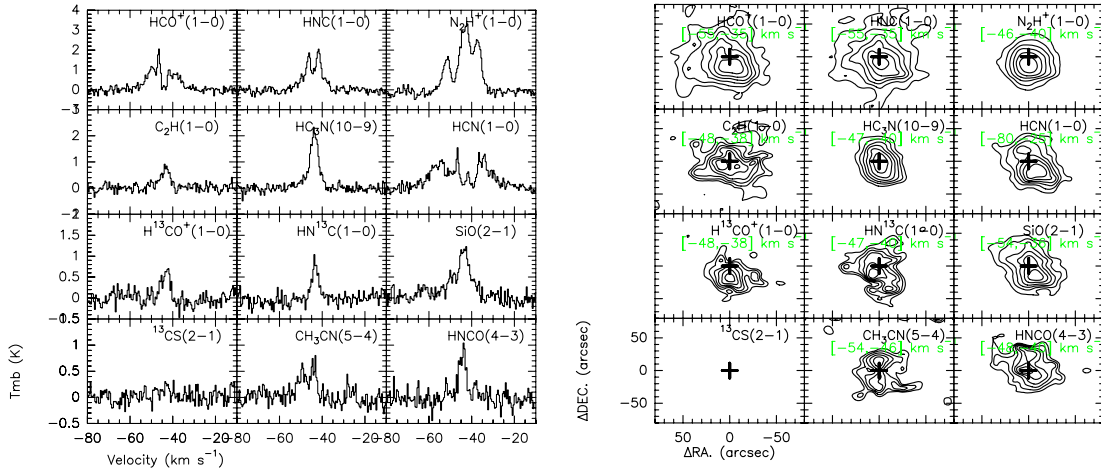


Fig. 6 Molecular spectra and integrated intensities of AGAL329.029–00.206. Contour levels are 40, 50, . . . , 90 percent of the peak emissions. The black pluses mark the 870 μm emission peaks of AGAL329.029–00.206. The green numbers show the range of integrations.

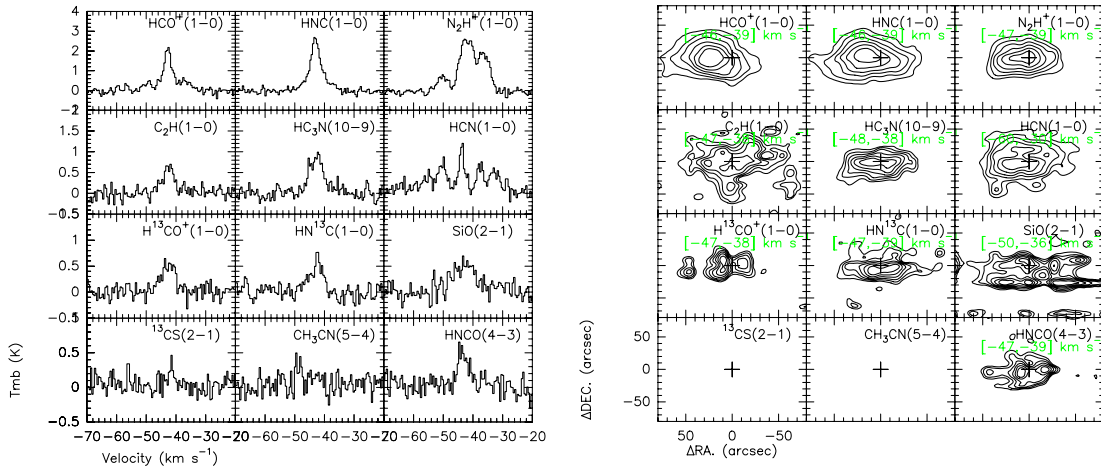


Fig. 7 Molecular spectra and integrated intensities of AGAL329.066–00.307. Contour levels are 40, 50, . . . , 90 percent of the peak emissions. The black pluses mark the 870 μm emission peaks of AGAL329.066–00.307. The green numbers show the range of integrations.

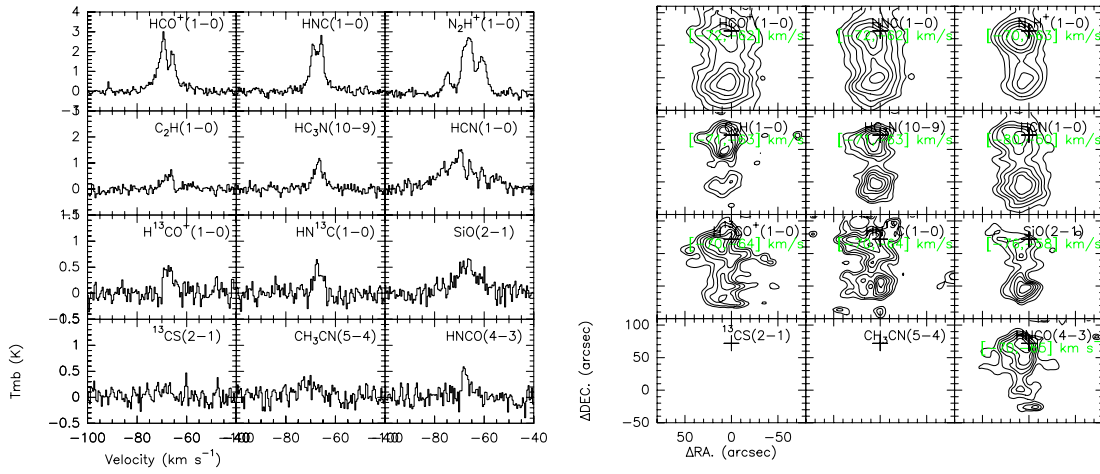


Fig. 8 Molecular spectra and integrated intensities of AGAL331.709+00.582. Contour levels are 40, 50, . . . , 90 percent of the peak emissions. The black pluses mark the 870 μm emission peaks of AGAL331.709+00.582. The green numbers show the range of integrations.

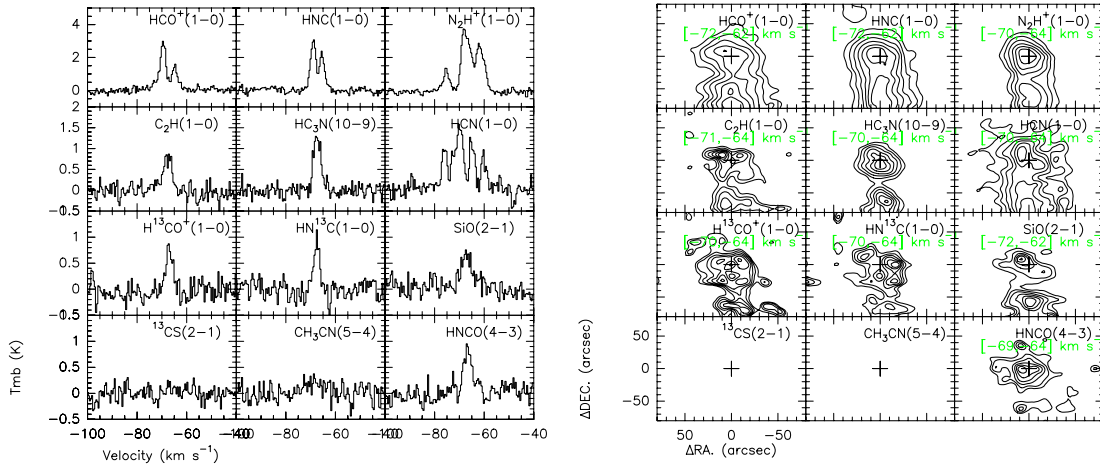


Fig. 9 Molecular spectra and integrated intensities of AGAL331.709+00.602. Contour levels are 40, 50, . . . , 90 percent of the peak emissions. The black pluses mark the 870 μm emission peaks of AGAL331.709+00.602. The green numbers show the range of integrations.

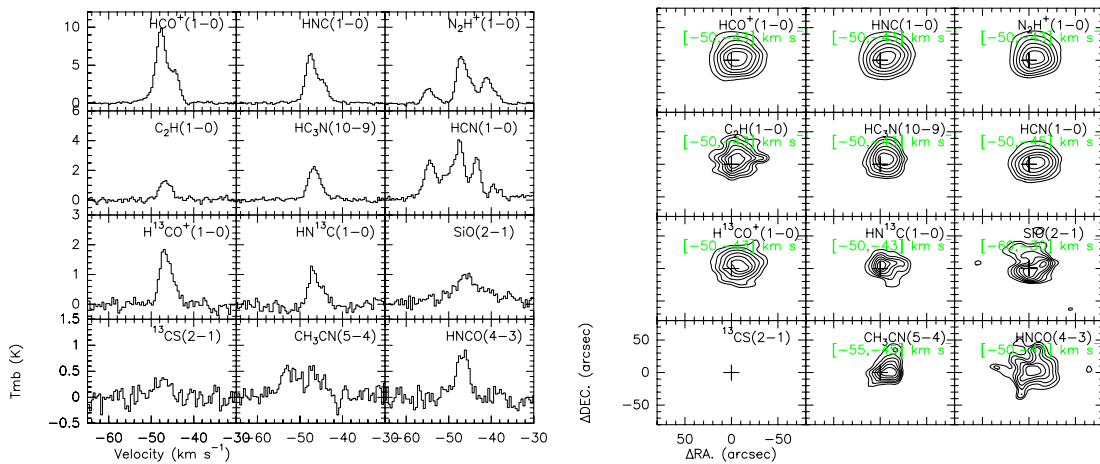


Fig. 10 Molecular spectra and integrated intensities of AGAL335.586-00.291. Contour levels are 40, 50, . . . , 90 percent of the peak emissions. The black pluses mark the 870 μm emission peaks of AGAL335.586-00.291. The green numbers show the range of integrations.

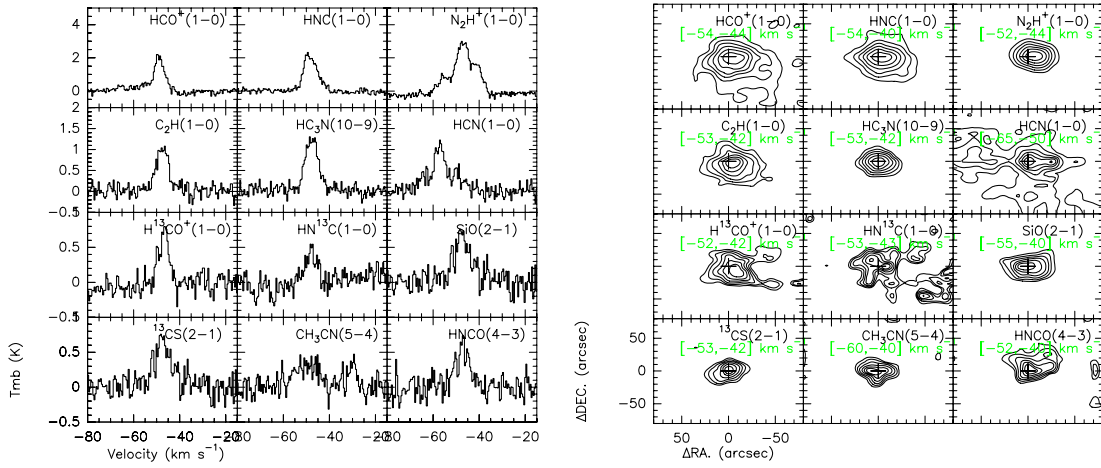


Fig. 11 Molecular spectra and integrated intensities of AGAL337.704–00.054. Contour levels are 40, 50, . . . , 90 percent of the peak emissions. The black pluses mark the 870 μm emission peaks of AGAL337.704–00.054. The green numbers show the range of integrations.

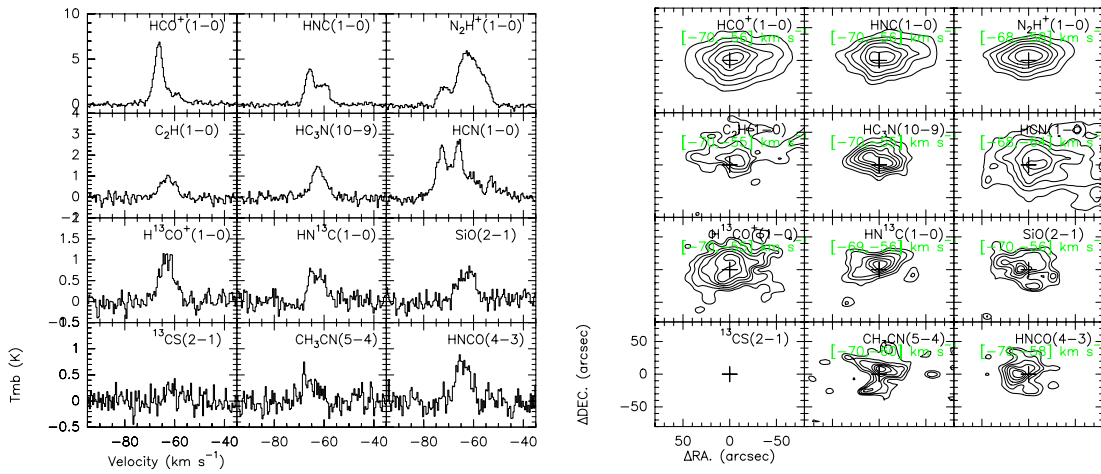


Fig. 12 Molecular spectra and integrated intensities of AGAL338.926+00.554. Contour levels are 40, 50, . . . , 90 percent of the peak emissions. The black pluses mark the 870 μm emission peak of AGAL338.926+00.554. The green numbers show the range of integrations.

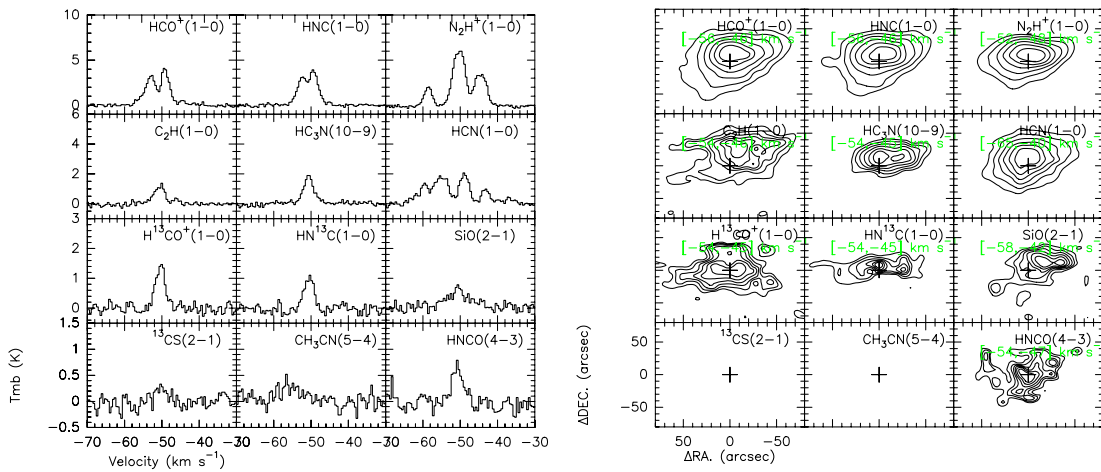


Fig. 13 Molecular spectra and integrated intensities of AGAL340.248-00.374. Contour levels are 40, 50, . . . , 90 percent of the peak emissions. The black pluses mark the 870 μm emission peaks of AGAL340.248-00.374. The green numbers show the range of integrations.

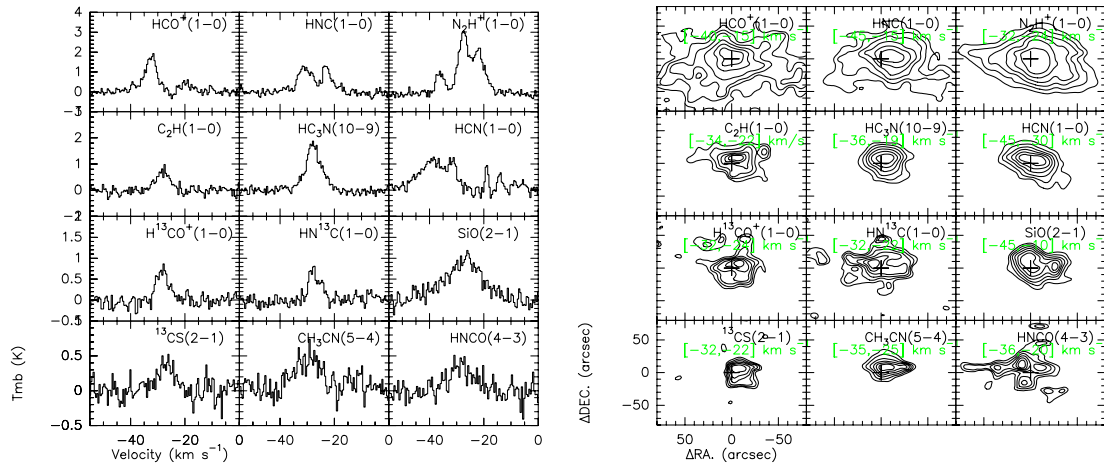


Fig. 14 Molecular spectra and integrated intensities of AGAL345.003-00.224. Contour levels are 40, 50, . . . , 90 percent of the peak emissions. The black pluses mark the 870 μm emission peaks of AGAL345.003-00.224. The green numbers show the range of integrations.

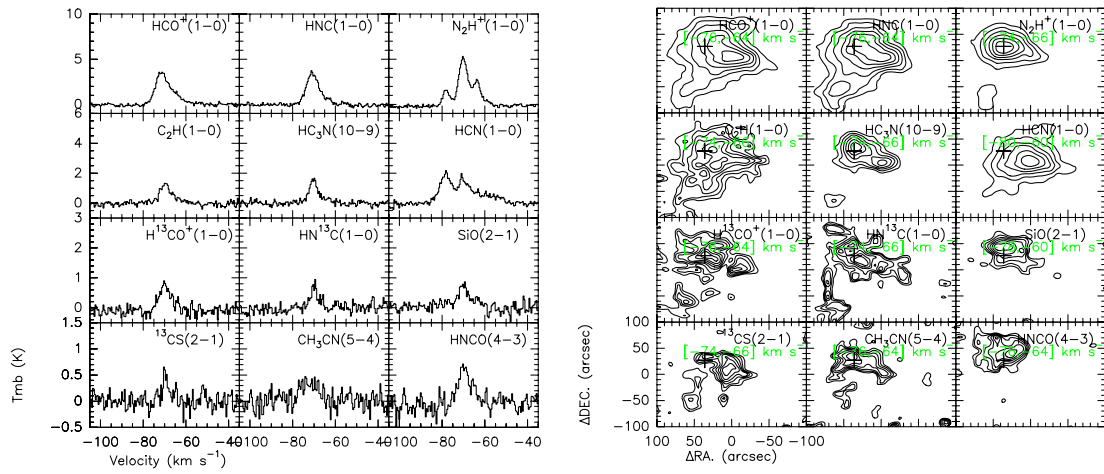


Fig. 15 Molecular spectra and integrated intensities of AGAL350.111+00.089. Contour levels are 40, 50, . . . , 90 percent of the peak emissions. The black pluses mark the 870 μm emission peaks of AGAL350.111+00.089. The green numbers show the range of integrations.

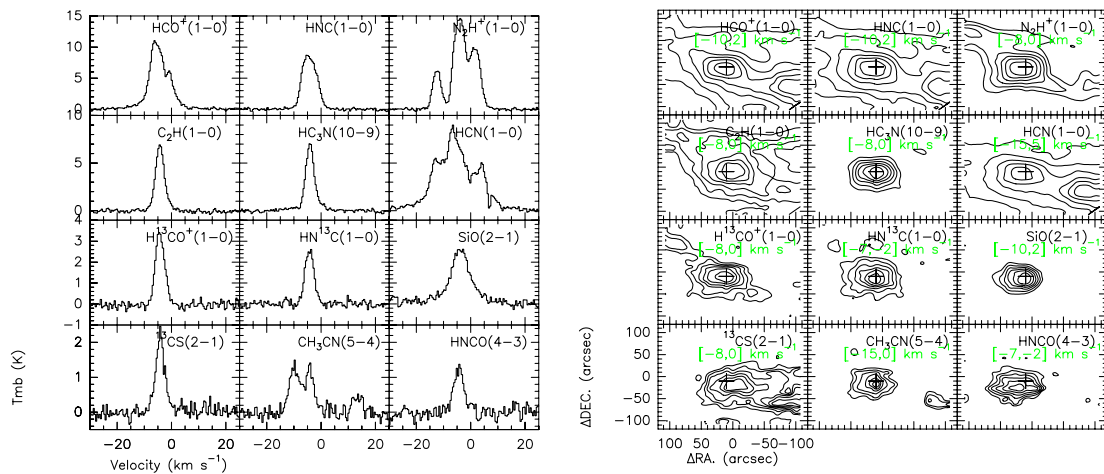


Fig. 16 Molecular spectra and integrated intensities of AGAL351.444+00.659. Contour levels are 40, 50, . . . , 90 percent of the peak emissions. The black pluses mark the 870 μm emission peaks of AGAL351.444+00.659. The green numbers show the range of integrations.

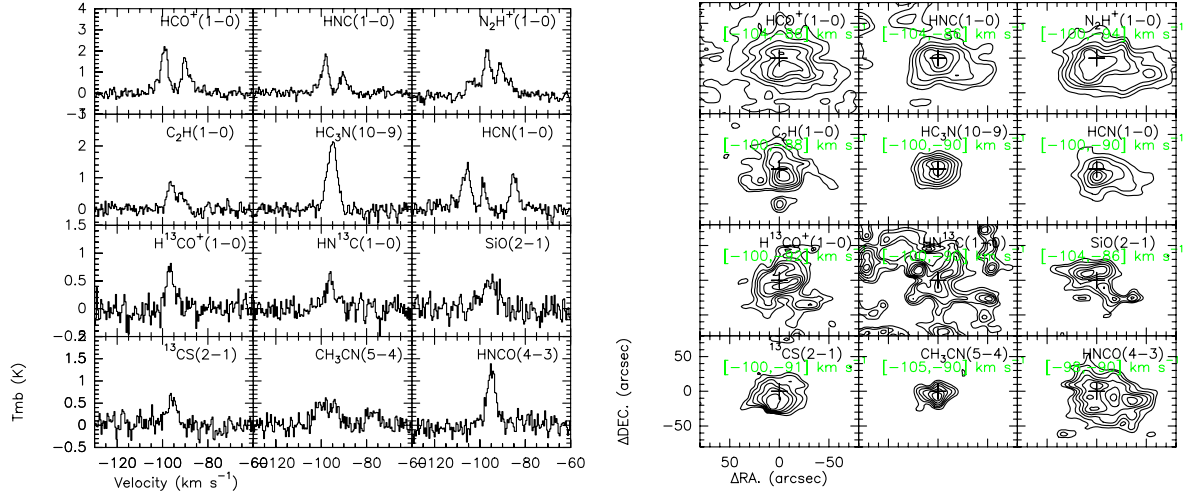


Fig. 17 Molecular spectra and integrated intensities of AGAL351.581–00.352. Contour levels are 40, 50, . . . , 90 percent of the peak emissions. The black pluses mark the 870 μm emission peaks of AGAL351.581–00.352. The green numbers show the range of integrations.

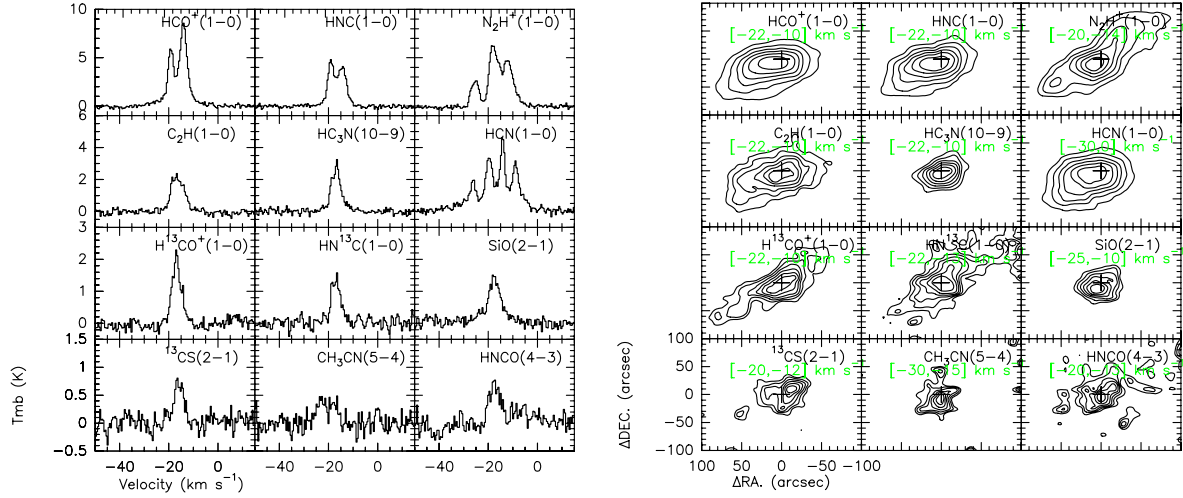


Fig. 18 Molecular spectra and integrated intensities of AGAL353.409–00.361. Contour levels are 40, 50, . . . , 90 percent of the peak emissions. The black pluses mark the 870 μm emission peaks of AGAL353.409–00.361. The green numbers show the range of integrations.

In many cases, the HCO^+ (1–0) and HNC (1–0) lines show wide wing emissions and so-called “blue profiles,” indicating outflow and infall activities on a large scale. Near 90 GHz, N_2H^+ (1–0) has seven hyperfine transitions. These transitions blend into three groups because of turbulence. The HCN (1–0) rotational transition splits into three hyperfine structures. However, as shown in the figures, these components always exhibit extended wing emissions, and their self-absorbed line profiles used to be blended, preventing us from doing the following analysis. The H^{13}CO^+ (1–0) and ^{13}CS (1–0), especially ^{13}CS (1–0), seem to be depleted in several sources. In the survey of MALT90, there are five CH_3CN (5–4) hyperfine transitions. However, the two components CH_3CN (5₀–

4₀) and (5₁–4₁) are always blended. Only in the source AGAL327.293–00.579 are all the five components distinctly detected.

Assuming local thermodynamic equilibrium (LTE) conditions and a beam filling factor of 1, we estimate column densities of HNCO , HC_3N , N_2H^+ , HNC , ^{13}CS , C_2H , H^{13}CO^+ and SiO by using equation

$$N(\text{species}) = \frac{8\pi\nu^3}{c^3 R} \frac{Q_{\text{rot}}}{g_u A_{ul}} \frac{\exp(E_l/kT_{\text{ex}})}{1 - \exp(-h\nu/kT_{\text{ex}})} \frac{\int T_{\text{mb}} dv}{1 - \exp(-\tau) J(T_{\text{ex}}) - J(T_{\text{bg}})}, \quad (2)$$

where c is the speed of light in a vacuum, ν is the frequency of the transitions, g_u is the statistical weight of

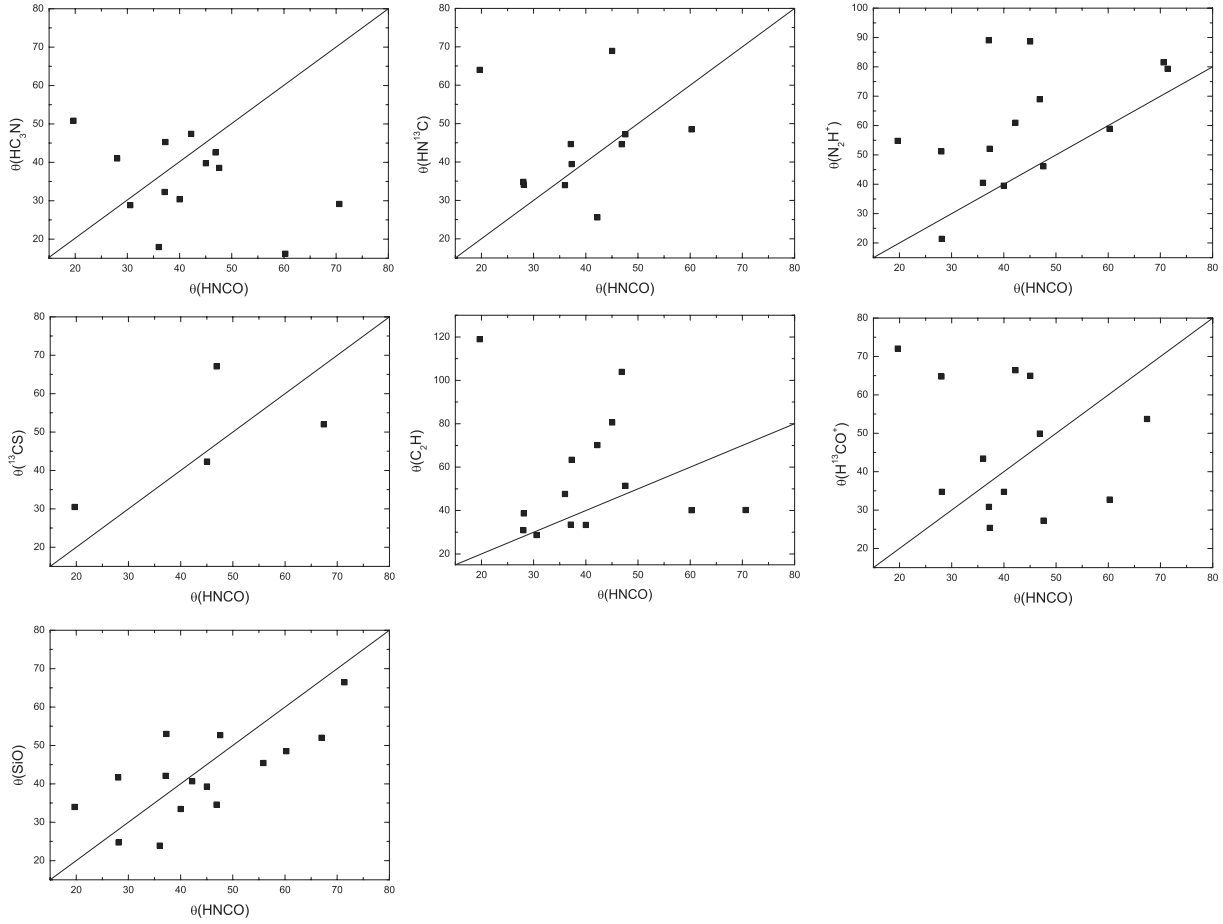


Fig. 19 Beam deconvolved angular diameters of HNC0 versus those of other species. The black lines indicate unity.

Table 2 The Beam Deconvolved Angular Diameters of Molecular Clouds

Source name	$\theta(\text{HNC0})$	$\theta(\text{HC}_3\text{N})$	$\theta(\text{N}_2\text{H}^+)$	$\theta(\text{HN}^{13}\text{C})$	$\theta(^{13}\text{CS})$	$\theta(\text{C}_2\text{H})$	$\theta(\text{H}^{13}\text{CO}^+)$	$\theta(\text{SiO})$
	(arcsec)							
AGAL008.671–00.356	71.38	...	79.34	66.45
AGAL008.684–00.367
AGAL010.472+00.027	60.26	16.18	58.91	37.29	...	40.13	32.72	46.62
AGAL318.948–00.197	36.00	17.93	40.50	33.96	...	47.65	43.41	23.90
AGAL327.293–00.579	19.66	50.85	54.79	63.99	30.46	118.96	72.04	33.96
AGAL329.029–00.206	47.58	38.55	46.13	47.21	...	51.43	27.26	52.69
AGAL329.066–00.307	37.29	45.28	52.12	39.46	...	63.39	25.35	53.07
AGAL331.709+00.582
AGAL331.709+00.602	30.55	28.85	28.74	...	12.44
AGAL335.586–00.291	39.99	30.36	39.54	8.78	...	33.34	34.74	33.43
AGAL337.704–00.054	28.11	11.97	21.40	34.13	...	38.70	34.74	24.74
AGAL338.926+00.554	28.02	41.01	51.20	34.83	...	30.94	64.78	41.66
AGAL340.248–00.374	42.22	47.40	60.95	25.58	...	70.15	66.42	40.65
AGAL345.003–00.224	37.13	32.25	89.05	44.67	6.91	33.53	30.84	42.09
AGAL350.111+00.089	55.86	45.42
AGAL351.444+00.659	46.90	42.58	68.95	44.63	67.12	103.89	49.91	34.58
AGAL351.581–00.352	67.40	29.16	81.56	...	52.00	40.21	53.73	39.15
AGAL353.409–00.361	45.03	39.77	88.64	68.92	42.30	80.64	64.96	39.32

the upper level, A_{ul} is the Einstein coefficient, E_1 is the energy of the lower level, Q_{rot} is the partition function, τ is the optical depth, and T_{bg} (2.73 K) and T_{ex} are the temperature of the background radiation and the excitation temperature in all cases respectively. We assume that T_{ex} is equal to the dust temperature (T_d) derived by Guzmán et al. (2015) (Table 1). R is only relevant for hyperfine transitions because it takes into account the satellite lines corrected by their relative opacities. The value of R is 5/9 for N_2H^+ , 5/12 for C_2H and 1.0 for transitions without hyperfine structure. The values of g_u , A_{ul} and E_1 can be found in the Cologne Database for Molecular Spectroscopy (CDMS) (Müller et al. 2001, 2005). $J(T)$ is defined by

$$J(T) = \frac{h\nu}{k} \frac{1}{e^{h\nu/kT} - 1}. \quad (3)$$

The partition functions (Q_{rot}) of the linear, rigid rotor molecules (N_2H^+ , $H^{13}CO^+$, HNC and SiO) can be approximated as

$$Q_{rot} \simeq \frac{kT_{ex}}{hB} + \frac{1}{3}, \quad (4)$$

where B is the rotational constant. The partition functions of C_2H , HC_3N and HNCO can be found in table 7 of Sanhueza et al. (2012).

We assume emissions of ^{13}CS , HC_3N , SiO and HNCO are optically thin. This assumption is suitable as shapes of these lines are relatively simple in all sources. To derive the line parameters, we fit these line emissions with a single Gaussian profile from the averaged pixels inside $38''$. The line widths, peak emissions and integrated intensities are listed in Table 3, 4 and 5 respectively. The derived column densities are listed in Table 6.

For HCO^+ and HNC, the presence of their isotopologues allows us to estimate their optical thickness through

$$\frac{1 - e^{-\tau_{12}}}{1 - e^{-\tau_{12}/X}} = \frac{^{12}T_{mb}}{^{13}T_{mb}}, \quad (5)$$

where $X \sim [^{12}C]/[^{13}C]$ is the isotope abundance ratio. Here we use a constant $X = 50$ in our calculations (Purcell et al. 2006).

In the case of N_2H^+ , we follow the procedure described by Purcell et al. (2009) to estimate the optical depth. Assuming the line widths of the individual hyperfine components of N_2H^+ are all equal and optically thin, the integrated intensities of group 1/group 2 (defined by Purcell et al. 2009) should have a ratio of 1:5. The optical depth can then be derived from the ratio of the two

integrated intensities, using the following equation

$$\frac{\int T_{MB,1} dv}{\int T_{MB,2} dv} = \frac{1 - \exp(-0.2\tau_2)}{1 - \exp(-\tau_2)}. \quad (6)$$

To derive the line intensities and peak emissions, we fit the three groups with three Gaussian profiles. The integrated intensities of group 2 are listed in Table 5 and the derived column densities of N_2H^+ are presented in Table 6.

Near 90 GHz, C_2H ($N = 1 - 0$) splits into six hyperfine transitions out of which two ($N = 1 - 0$, $J = 3/2 - 1/2$, $F = 2 - 1$ and $N = 1 - 0$, $J = 3/2 - 1/2$, $F = 1 - 0$) could easily be detected. The optical depth of C_2H ($F = 2 - 1$) can then be derived by comparing with its hyperfine components. In the case of the optically thin limit, the intensity ratio of C_2H ($F = 2 - 1$) and C_2H ($F = 1 - 0$) should be 2.0 (Tucker et al. 1974). Thus, the opacity of C_2H ($F = 2 - 1$) can be given by

$$\frac{1 - e^{-0.5\tau}}{1 - e^{-\tau}} = \frac{T_{mb}(F = 1 - 0)}{T_{mb}(F = 2 - 1)}. \quad (7)$$

The column densities of C_2H can then be calculated through Equation (1). The calculated values are listed in Table 6.

To transform column densities to abundances, we use the $N(\text{species})/N(H_2)$ ratio, where $N(H_2)$ values were estimated by Guzmán et al. (2015) (Table 1). The derived abundances are presented in Table 7.

4 ANALYSIS

Figure 20 shows correlation plots of the HNCO abundance versus those of other species. Table 8 presents the least-squares fitting functions and coefficients for the correlations between HNCO and these species. It can be noted that in our sample, the abundances of HC_3N , HNC, N_2H^+ , C_2H and $H^{13}CO^+$ have a good correlation with $\chi(\text{HNCO})$. However, the correlations between $\chi(\text{HNCO})$ and $\chi(^{13}CS)$, $\chi(\text{SiO})$ are not so good. We should mention here that the beam size of Mopra is $38''$, which at a distance of 3 kpc for high-mass star-forming regions, has a physical size of ~ 0.6 pc. Therefore, our data probe star forming clumps, which may contain several star-forming cores (size < 0.1 pc), and also diffuse material.

HC_3N is regarded as a good tracer of warm dense gas (e.g. Miettinen 2014). Using the PMO 13.7 m telescope, Li et al. (2013) studied spatial distributions of HNCO in nine massive star-forming regions. They found the integrated intensities, line widths and LSR velocities of HC_3N and HNCO correlate well with each other.

Table 3 Line Widths Of Species

Source name	HNC0	HC ₃ N	N ₂ H ⁺	HN ¹³ C	¹³ CS	C ₂ H	H ¹³ CO ⁺	SiO
(1)	(2)	(3)	(4)	(5)	(6)	(7)	(8)	(9)
AGAL008.671–00.356	6.24 (0.54)	4.48 (0.14)	3.47 (0.09)	4.33 (0.31)	5.20 (0.77)	5.25 (0.35)	2.38 (0.24)	...
AGAL008.684–00.367	6.66 (0.69)	3.65 (0.16)	5.31 (0.09)	4.66 (0.47)	...	4.59 (0.32)	4.21 (0.28)	...
AGAL010.472+00.027	6.52 (0.65)	7.24 (0.26)	4.76 (0.37)	6.74 (0.64)	7.87 (0.78)	7.75 (0.45)	6.37 (0.42)	6.34 (0.72)
AGAL318.948–00.197	4.56 (0.79)	3.07 (0.17)	3.06 (0.05)	3.02 (0.49)	3.06 (0.64)	2.76 (0.19)	2.63 (0.17)	8.55 (0.81)
AGAL327.293–00.579	5.45 (0.65)	5.89 (0.10)	5.56 (0.18)	5.14 (0.30)	6.18 (0.21)	6.20 (0.20)	4.99 (0.25)	7.54 (0.46)
AGAL329.029–00.206	3.85 (0.36)	4.90 (0.17)	5.79 (0.17)	3.37 (0.34)	...	5.13 (0.54)	4.50 (0.45)	10.31 (0.65)
AGAL329.066–00.307	4.41 (0.51)	5.39 (0.43)	5.42 (0.19)	5.51 (0.60)	...	4.27 (0.50)	5.98 (0.64)	9.79 (0.97)
AGAL331.709+00.582	2.76 (0.49)	4.83 (0.33)	5.01 (0.14)	3.71 (0.45)	...	4.37 (0.55)	4.06 (0.51)	12.07 (1.33)
AGAL331.709+00.602	4.42 (0.57)	3.45 (0.18)	3.94 (0.09)	2.60 (0.30)	...	4.08 (0.44)	3.39 (0.38)	6.02 (0.76)
AGAL335.586–00.291	3.52 (0.33)	3.54 (0.12)	3.27 (0.05)	3.41 (0.29)	...	3.40 (0.22)	3.55 (0.15)	12.43 (0.90)
AGAL337.704–00.054	7.19 (0.69)	6.72 (0.28)	6.21 (0.43)	5.98 (0.65)	5.75 (0.74)	6.70 (0.39)	4.87 (0.40)	8.96 (0.80)
AGAL338.926+00.554	6.46 (0.53)	6.42 (0.31)	7.78 (0.36)	7.02 (0.56)	...	6.83 (0.46)	7.30 (0.46)	8.28 (0.66)
AGAL340.248–00.374	3.97 (0.40)	3.28 (0.14)	3.78 (0.08)	2.95 (0.22)	...	3.64 (0.29)	2.94 (0.18)	8.27 (0.89)
AGAL345.003–00.224	10.96 (1.14)	6.95 (0.20)	4.10 (0.14)	5.26 (0.39)	7.39 (1.03)	6.14 (0.47)	5.58 (0.46)	16.78 (0.78)
AGAL350.111+00.089	7.33 (0.66)	5.52 (0.39)	4.67 (0.10)	5.11 (0.56)	2.29 (0.56)	7.84 (0.45)	6.78 (0.53)	9.53 (1.15)
AGAL351.444+00.659	4.69 (0.31)	3.98 (0.06)	4.65 (0.43)	3.78 (0.11)	4.05 (0.16)	3.94 (0.05)	3.99 (0.08)	8.35 (0.21)
AGAL351.581–00.352	4.9 (0.33)	5.15 (0.15)	3.13 (0.20)	5.80 (1.05)	5.11 (0.67)	7.30 (0.64)	5.36 (0.59)	8.35 (1.01)
AGAL353.409–00.361	5.95 (0.42)	4.81 (0.13)	5.00 (0.43)	4.72 (0.27)	4.61 (0.43)	6.47 (0.24)	4.46 (0.17)	7.15 (0.41)

Table 4 Peak Intensities of Species

Source name	HNC0	HC ₃ N	N ₂ H ⁺	HN ¹³ C	¹³ CS	C ₂ H	H ¹³ CO ⁺	SiO
(1)	(2)	(3)	(4)	(5)	(6)	(7)	(8)	(9)
AGAL008.671–00.356	0.78	2.25	4.51	1.04	0.52	1.40	1.33	...
AGAL008.684–00.367	0.65	2.04	3.46	0.85	...	1.08	1.01	...
AGAL010.472+00.027	0.55	1.37	2.19	0.54	0.51	0.99	0.77	0.52
AGAL318.948–00.197	0.41	1.62	5.06	0.67	0.35	1.39	1.42	0.62
AGAL327.293–00.579	0.61	3.52	5.38	0.93	1.52	2.29	1.38	1.14
AGAL329.029–00.206	0.88	2.09	3.33	0.84	...	0.76	0.67	0.97
AGAL329.066–00.307	0.50	0.89	2.75	0.59	...	0.61	0.56	0.52
AGAL331.709+00.582	0.55	0.97	2.86	0.52	...	0.55	0.50	0.50
AGAL331.709+00.602	0.85	1.32	3.81	0.95	...	0.82	0.84	0.63
AGAL335.586–00.291	0.87	2.18	6.10	1.08	...	1.30	1.78	0.76
AGAL337.704–00.054	0.55	1.28	3.13	0.44	0.53	1.07	0.72	0.64
AGAL338.926+00.554	0.79	1.41	5.82	0.71	...	0.94	1.08	0.73
AGAL340.248–00.374	0.70	1.81	6.60	1.07	...	1.18	1.43	0.53
AGAL345.003–00.224	0.34	1.67	2.91	0.68	0.39	0.74	0.76	0.93
AGAL350.111+00.089	0.64	1.51	5.25	0.69	0.51	1.22	0.83	0.59
AGAL351.444+00.659	1.27	7.54	15.06	2.60	2.14	6.85	3.47	2.43
AGAL351.581–00.352	1.25	2.11	1.94	0.48	0.59	0.68	0.76	0.46
AGAL353.409–00.361	0.73	2.73	6.03	1.39	0.73	2.25	1.97	1.31

On the other hand, also based on the data of MALT90, Miettinen (2014) found that in some infrared dark clouds (IRDCs), the emission morphology of HC₃N resembles those of HNC0, HNC and N₂H⁺. These studies imply HC₃N has a similar excitation mechanism as HNC0. As shown in the top-left panel of Figure 20, there is a

hint that the abundance of HC₃N increases as a function of $\chi(\text{HNC0})$. The functional form of the linear fit is $\chi(\text{HC}_3\text{N}) = 0.89 + 0.24 \chi(\text{HNC0})$. Previous studies indicate HC₃N is mainly produced through $\text{C}_2\text{H}_2 + \text{CN} \rightarrow \text{HC}_3\text{N} + \text{H}$ in star-forming regions (Chapman et al. 2009). CN is also the main material to produce HNC0.

Table 5 Integrated Intensities of Species

Source name	HNCO	HC ₃ N	N ₂ H ⁺	HN ¹³ C	¹³ CS	C ₂ H	H ¹³ CO ⁺	SiO
(1)	(2)	(3)	(4)	(5)	(6)	(7)	(8)	(9)
AGAL008.671–00.356	5.22 (0.37)	10.77 (0.29)	16.67 (0.69)	4.81 (0.29)	2.91 (0.32)	7.87 (0.41)	3.39 (0.69)	...
AGAL008.684–00.367	4.64 (0.40)	7.95 (0.27)	19.59 (0.02)	4.24 (0.34)	...	5.32 (0.33)	4.56 (0.28)	...
AGAL010.472+00.027	3.88 (0.33)	10.58 (0.32)	11.13 (1.58)	3.93 (0.32)	4.30 (0.36)	8.17 (0.39)	5.26 (0.31)	3.54 (0.34)
AGAL318.948–00.197	2.02 (0.29)	5.30 (0.25)	16.52 (0.25)	2.16 (0.26)	1.49 (0.24)	4.09 (0.23)	3.98 (0.22)	5.67 (0.42)
AGAL327.293–00.579	3.57 (0.33)	22.12 (0.33)	31.95 (1.66)	5.14 (0.28)	10.01 (0.31)	15.13 (0.44)	7.34 (0.33)	9.22 (0.46)
AGAL329.029–00.206	3.63 (0.29)	10.91 (0.31)	20.55 (0.53)	3.03 (0.25)	...	4.17 (0.35)	3.22 (0.30)	10.73 (0.51)
AGAL329.066–00.307	2.39 (0.23)	4.96 (0.33)	15.91 (0.55)	3.49 (0.30)	...	2.78 (0.25)	3.57 (0.32)	5.42 (0.42)
AGAL331.709+00.582	1.64 (0.21)	4.62 (0.27)	15.25 (0.37)	2.08 (0.23)	...	2.57 (0.27)	2.19 (0.25)	6.50 (0.55)
AGAL331.709+00.602	4.03 (0.38)	4.87 (0.23)	16.00 (0.37)	2.65 (0.25)	...	3.59 (0.31)	3.04 (0.29)	4.05 (0.38)
AGAL335.586–00.291	3.26 (0.25)	8.22 (0.23)	21.24 (0.30)	3.94 (0.29)	...	4.72 (0.26)	6.75 (0.25)	10.13 (0.53)
AGAL337.704–00.054	4.21 (0.34)	9.20 (0.33)	20.73 (0.50)	2.83 (0.27)	3.29 (0.32)	7.63 (0.36)	3.78 (0.28)	6.15 (0.42)
AGAL338.926+00.554	5.48 (0.41)	9.65 (0.39)	48.24 (2.99)	5.33 (0.41)	...	6.85 (0.42)	8.44 (0.45)	6.45 (0.45)
AGAL340.248–00.374	2.97 (0.24)	6.33 (0.22)	26.60 (0.46)	3.38 (0.23)	...	4.57 (0.28)	4.48 (0.23)	4.75 (0.40)
AGAL345.003–00.224	4.08 (0.35)	12.42 (0.29)	12.74 (0.53)	3.82 (0.24)	3.09 (0.35)	4.88 (0.32)	4.56 (0.31)	16.66 (0.62)
AGAL350.111+00.089	5.06 (0.39)	8.88 (0.46)	26.17 (0.54)	3.78 (0.31)	1.26 (0.24)	10.19 (0.44)	6.04 (0.39)	6.01 (0.50)
AGAL351.444+00.659	6.34 (0.34)	32.02 (0.45)	74.65 (2.36)	10.49 (0.27)	9.20 (0.30)	28.78 (0.31)	14.79 (0.26)	21.64 (0.44)
AGAL351.581–00.352	6.53 (0.34)	11.58 (0.30)	6.49 (0.50)	2.98 (0.37)	3.21 (0.35)	5.30 (0.42)	4.35 (0.37)	4.11 (0.43)
AGAL353.409–00.361	4.63 (0.37)	14.02 (0.31)	32.11 (1.14)	6.99 (0.32)	3.59 (0.28)	15.51 (0.49)	9.40 (0.30)	9.99 (0.41)

Table 6 Column Densities of Species

Source name	HNCO	HC ₃ N	N ₂ H ⁺	HNC	¹³ CS	C ₂ H	H ¹³ CO ⁺	SiO
(1)	(2)	(10 ¹³ cm ⁻²)	(4)	(10 ¹⁴ cm ⁻²)	(10 ¹³ cm ⁻²)	(10 ¹⁵ cm ⁻²)	(10 ¹³ cm ⁻²)	(9)
AGAL008.671–00.356	9.63 (2.01)	4.33 (0.11)	9.75 (1.33)	7.69 (0.94)	2.13 (0.44)	1.40 (0.21)	6.19 (1.82)	...
AGAL008.684–00.367	8.77 (0.15)	3.19 (0.11)	5.55 (0.07)	9.66 (0.47)	...	1.12 (0.11)	8.51 (0.63)	...
AGAL010.472+00.027	9.05 (2.00)	4.29 (0.18)	7.66 (1.65)	7.30 (0.39)	3.70 (0.51)	1.00 (0.10)	10.57 (1.19)	1.81 (0.27)
AGAL318.948–00.197	3.98 (0.64)	2.12 (0.10)	3.43 (0.10)	5.28 (1.27)	1.14 (0.20)	0.44 (0.03)	7.82 (0.53)	2.59 (0.23)
AGAL327.293–00.579	7.73 (1.04)	8.91 (0.17)	8.53 (0.69)	10.94 (0.37)	8.19 (0.48)	2.19 (0.12)	16.22 (1.18)	4.49 (0.35)
AGAL329.029–00.206	5.53 (0.65)	4.55 (0.08)	6.78 (0.34)	11.72 (0.88)	...	0.63 (0.07)	5.69 (0.67)	4.14 (0.29)
AGAL329.066–00.307	3.46 (0.44)	2.10 (0.11)	2.51 (0.14)	3.48 (0.14)	...	0.67 (0.07)	5.60 (0.63)	2.02 (0.20)
AGAL331.709+00.582	2.43 (0.7)	1.92 (0.03)	2.32 (0.30)	3.78 (0.81)	...	0.51 (0.11)	3.31 (0.75)	2.46 (0.46)
AGAL331.709+00.602	6.30 (0.88)	2.01 (0.07)	3.59 (0.19)	5.41 (0.28)	...	0.53 (0.07)	5.06 (0.64)	1.59 (0.19)
AGAL335.586–00.291	5.64 (0.54)	3.32 (0.09)	5.98 (0.16)	5.12 (0.31)	...	0.46 (0.03)	10.91 (0.55)	4.26 (0.27)
AGAL337.704–00.054	7.32 (0.9)	3.72 (0.11)	5.34 (0.28)	4.02 (0.14)	2.31 (0.30)	1.46 (0.11)	7.10 (0.74)	2.59 (0.25)
AGAL338.926+00.554	8.50 (1.05)	4.00 (0.11)	7.60 (0.74)	6.02 (0.37)	...	1.03 (0.10)	12.88 (1.12)	2.52 (0.25)
AGAL340.248–00.374	5.03 (0.64)	2.57 (0.07)	5.53 (0.27)	7.77 (0.60)	...	0.58 (0.08)	8.27 (0.69)	1.96 (0.23)
AGAL345.003–00.224	8.10 (4.95)	4.98 (0.43)	4.51 (1.71)	12.60 (4.19)	2.38 (1.09)	0.58 (0.24)	9.93 (4.00)	7.67 (2.68)
AGAL350.111+00.089	9.33 (0.7)	3.57 (0.18)	6.57 (0.25)	8.93 (0.22)	0.92 (0.19)	1.05 (0.06)	10.92 (0.91)	2.63 (0.27)
AGAL351.444+00.659	10.74 (1.58)	13.01 (0.05)	24.60 (2.40)	22.23 (1.18)	6.37 (0.60)	3.61 (0.27)	26.43 (2.09)	8.97 (0.71)
AGAL351.581–00.352	12.05 (1.16)	4.65 (0.11)	5.72 (0.62)	3.93 (0.34)	2.35 (0.33)	1.86 (0.21)	8.52 (1.00)	1.80 (0.24)
AGAL353.409–00.361	8.18 (1.03)	5.66 (0.10)	10.07 (0.68)	14.06 (0.76)	2.56 (0.28)	2.28 (0.15)	16.43 (1.03)	4.26 (0.30)

In shocked gas, CN can form OCN through $\text{CN} + \text{O}_2 \rightarrow \text{OCN} + \text{O}$ (Turner et al. 1999). OCN can further produce HNCO both through gas-phase ($\text{OCN} + \text{H}_2 \rightarrow \text{HNCO} + \text{H}$) and/or grain surface reactions ($\text{OCN} + \text{H} \rightarrow \text{HNCO}$) (e.g. Allen & Robinson 1977, Turner et al.

1999). This may be the reason that the abundance of HC₃N increases as a function of $\chi(\text{HNCO})$. However, as mentioned above, in order to investigate the essential relationship between HNCO and HC₃N, high angular res-

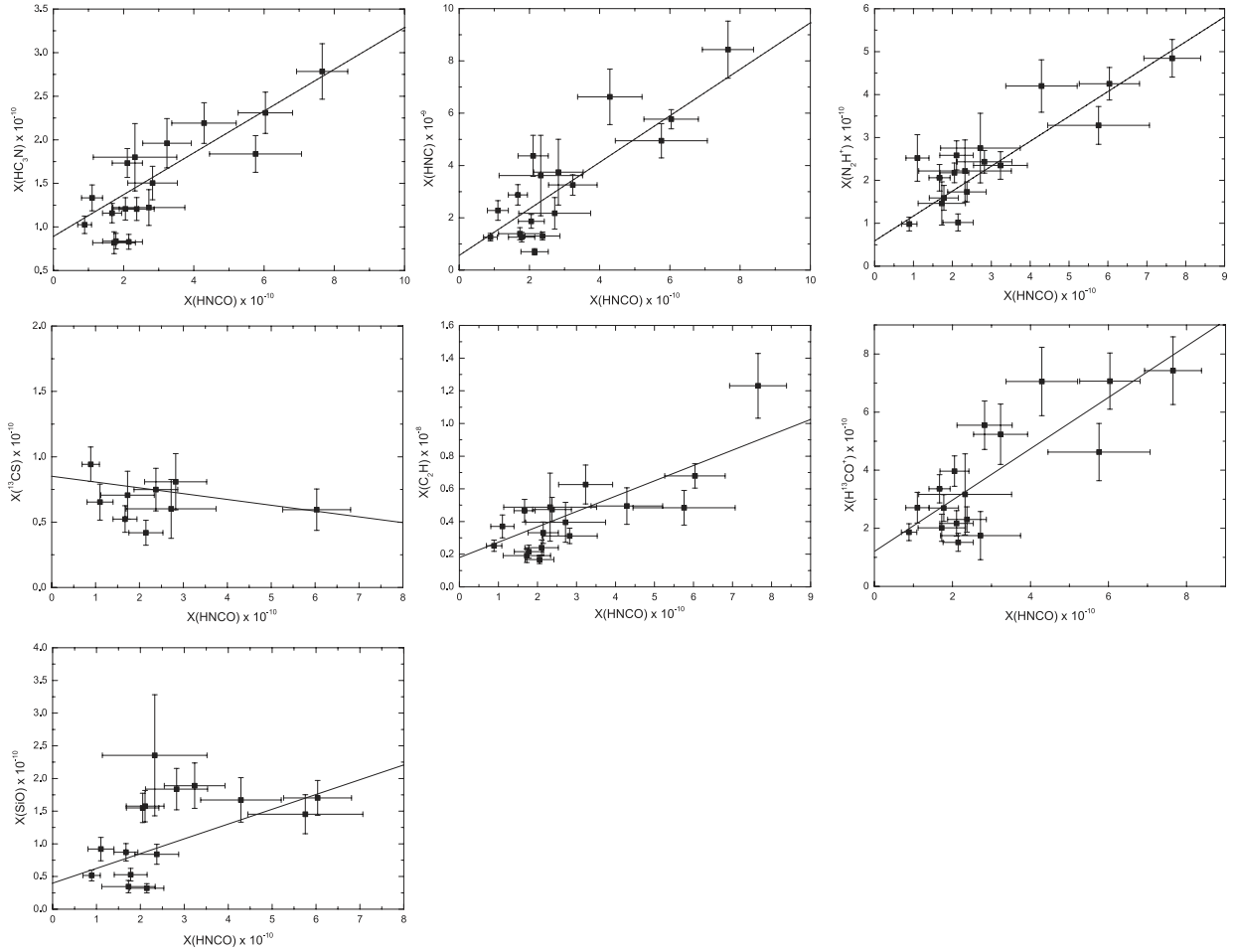


Fig. 20 Plots of the HNCO abundance versus those of other species. The solid line shows the least-squares fit to the data.

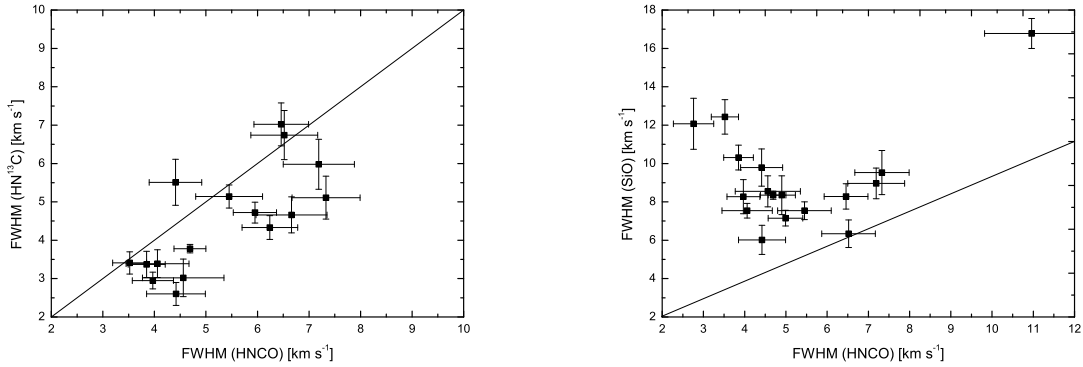


Fig. 21 Plots of the velocity width of HNCO versus those of HN^{13}C (left) and SiO (right). The black lines indicate unity.

olution observations and chemical models should be carried out in the future.

N_2H^+ is regarded as an excellent cold gas, as it is more resistant to freeze-out on grains than carbon-

bearing species (Bergin et al. 2001). Recently, we found that the abundance of N_2H^+ has a tight correlation with that of HNC, indicating that HNC may also be preferentially formed in cold gas (Yu & Xu 2016). In a sur-

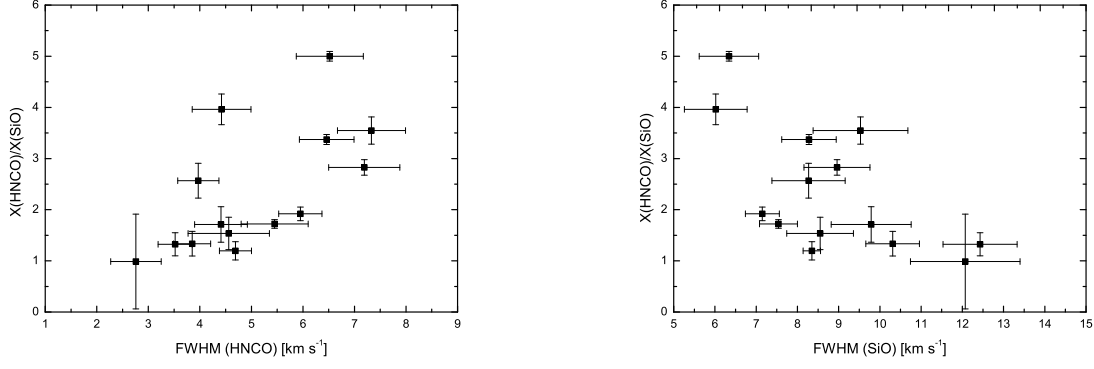


Fig. 22 *Left:* $\chi(\text{HNCO})/\chi(\text{SiO})$ relative abundance ratio plotted as a function of the HNCO velocity widths. *Right:* $\chi(\text{HNCO})/\chi(\text{SiO})$ relative abundance ratio plotted as a function of the SiO velocity widths.

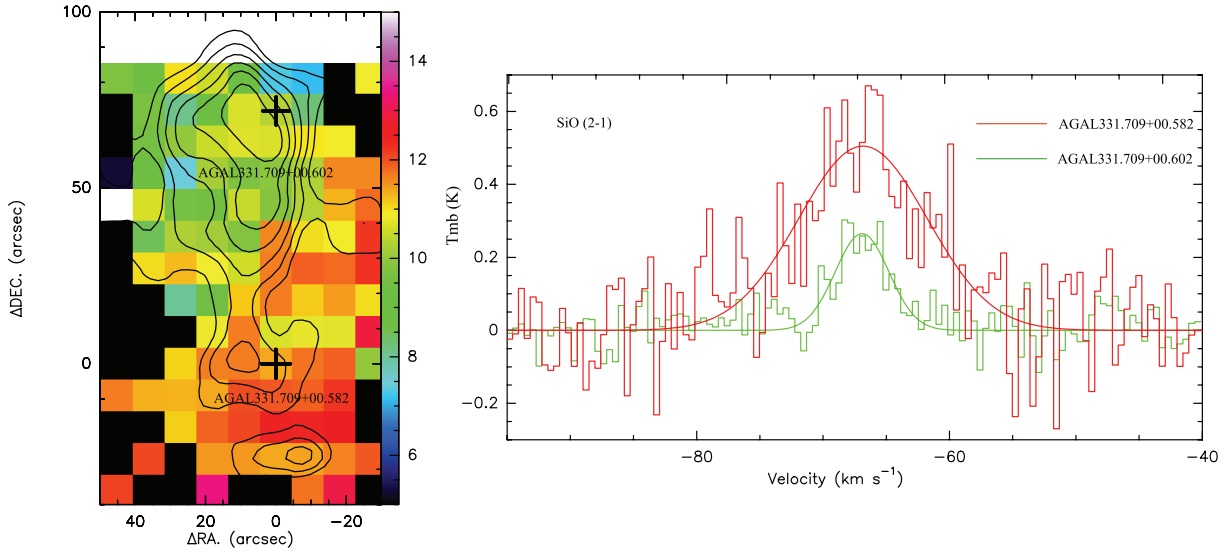


Fig. 23 *Left:* Velocity-width (moment 2) map of SiO overlaid with HNCO integrated intensity contours (*black*). The two pluses mark the center locations of AGAL331.709+00.602 and AGAL331.709+00.582. *Right:* Spectra of SiO in the center of the two clumps. The red and green lines are the Gaussian-fitted lines.

vey of 18 molecular clouds, Jackson et al. (1984) detected HNCO emissions in seven sources with an average excitation temperature of 12 K, indicating HNCO could also trace cold gas. The top-middle panel plots the HNC abundance as a function of $\chi(\text{HNCO})$. A least-squares fit to the data yields $\chi(\text{HNC}) = 0.56 + 0.89\chi(\text{HNCO})$. The top-right panel shows the N_2H^+ abundance as a function of $\chi(\text{HNCO})$ and the functional form of the linear fit is $\chi(\text{N}_2\text{H}^+) = 0.59 + 0.58\chi(\text{HNCO})$.

SiO is a well-known shocked gas tracer (e.g. Schilke et al. 1997). In the ambient gas of energetic young outflows, the abundance of SiO could jump to almost 10^{-6} (Martin-Pintado et al. 1992). The previous SiO production mechanism explains spectral lines that show ex-

tended wing emission, which is caused by the interaction between high-velocity shocks (typically C-shocks with $v > 25 \text{ km s}^{-1}$ and/or fast J-shocks) and the surrounding medium. There is also increasing evidence of SiO emission as a tracer of low-velocity ($< 10 \text{ km s}^{-1}$) both in observations and modeling (e.g. Jiménez-Serra et al. 2010; Louvet et al. 2016). Jiménez-Serra et al. (2010) detected extended narrow SiO emission (line width of $\sim 0.8 \text{ km s}^{-1}$) not associated with signs of star formation in an IRDC. They suggest this narrow line emission of SiO could be generated by the following processes: i) remnants of large-scale shocks caused by the formation process of the IRDC; ii) decelerated gas in large-scale outflows driven by neighboring massive protostars;

Table 7 Abundances of Species

Source name	HNC0	HC ₃ N (10 ⁻¹⁰)	N ₂ H ⁺	HNC (10 ⁻⁹)	¹³ CS (10 ⁻¹⁰)	C ₂ H (10 ⁻⁸)	H ¹³ CO ⁺ (10 ⁻¹⁰)	SiO
(1)	(2)	(3)	(4)	(5)	(6)	(7)	(8)	(9)
AGAL008.671–00.356	2.72 (1.02)	1.22 (0.21)	2.75 (0.81)	2.17 (0.60)	0.60 (0.23)	0.40 (0.12)	1.75 (0.83)	...
AGAL008.684–00.367	7.65 (0.73)	2.78 (0.32)	4.84 (0.44)	8.43 (1.09)	...	0.98 (0.20)	7.43 (1.16)	...
AGAL010.472+00.027	1.73 (0.61)	0.82 (0.13)	1.46 (0.50)	1.39 (0.23)	0.71 (0.18)	0.19 (0.04)	2.02 (0.47)	0.35 (0.09)
AGAL318.948–00.197	2.82 (0.71)	1.50 (0.19)	2.43 (0.26)	3.75 (1.26)	0.81 (0.22)	0.31 (0.05)	5.55 (0.83)	1.84 (0.32)
AGAL327.293–00.579	0.89 (0.20)	1.03 (0.10)	0.98 (0.16)	1.26 (0.14)	0.94 (0.13)	0.25 (0.03)	1.87 (0.29)	0.52 (0.08)
AGAL329.029–00.206	2.11 (0.43)	1.73 (0.17)	2.58 (0.34)	4.37 (0.79)	...	0.24 (0.05)	2.17 (0.44)	1.58 (0.24)
AGAL329.066–00.307	3.24 (0.69)	1.96 (0.28)	2.35 (0.32)	3.25 (0.39)	...	0.63 (0.12)	5.24 (1.04)	1.89 (0.35)
AGAL331.709+00.582	2.33 (1.19)	1.80 (0.39)	2.22 (0.72)	3.62 (1.54)	...	0.49 (0.21)	3.17 (1.39)	2.35 (0.93)
AGAL331.709+00.602	5.76 (1.31)	1.84 (0.21)	3.28 (0.44)	4.94 (0.66)	...	0.48 (0.11)	4.62 (0.99)	1.45 (0.30)
AGAL335.586–00.291	2.05 (0.37)	1.21 (0.13)	2.18 (0.23)	1.86 (0.26)	...	0.17 (0.02)	3.97 (0.52)	1.55 (0.23)
AGAL337.704–00.054	2.37 (0.50)	1.21 (0.13)	1.73 (0.23)	1.30 (0.15)	0.75 (0.16)	0.47 (0.07)	2.30 (0.44)	0.84 (0.15)
AGAL338.926+00.554	1.78 (0.37)	0.84 (0.09)	1.59 (0.29)	1.26 (0.18)	...	0.22 (0.04)	2.70 (0.46)	0.53 (0.10)
AGAL340.248–00.374	4.29 (0.92)	2.19 (0.23)	4.72 (0.61)	6.63 (1.06)	...	0.49 (0.11)	7.05 (1.18)	1.67 (0.34)
AGAL345.003–00.224	2.40 (2.81)	1.47 (0.69)	1.33 (1.15)	3.73 (2.97)	0.70 (0.68)	0.17 (0.16)	2.94 (2.62)	2.27 (1.86)
AGAL350.111+00.089	6.04 (0.77)	2.31 (0.24)	4.25 (0.38)	5.77 (0.37)	0.60 (0.16)	0.68 (0.07)	7.07 (0.97)	1.70 (0.27)
AGAL351.444+00.659	1.10 (0.30)	1.33 (0.15)	2.52 (0.54)	2.28 (0.38)	0.65 (0.14)	0.37 (0.07)	2.71 (0.53)	0.92 (0.18)
AGAL351.581–00.352	2.15 (0.39)	0.83 (0.08)	1.02 (0.20)	0.70 (0.12)	0.42 (0.10)	0.33 (0.07)	1.52 (0.31)	0.32 (0.07)
AGAL353.409–00.361	1.67 (0.27)	1.16 (0.11)	2.06 (0.31)	2.88 (0.39)	0.52 (0.10)	0.47 (0.07)	3.36 (0.49)	0.87 (0.13)

Table 8 Linear Fitting Results for the Correlation between HNC0 and Other Species

No.	Linear fitting functions	Pearson correlation coefficient
1	$\chi(\text{HC}_3\text{N}) = 0.89 + 0.24 \chi(\text{HNC0})$	0.85
2	$\chi(\text{HNC}) = 0.56 + 0.89 \chi(\text{HNC0})$	0.86
3	$\chi(\text{N}_2\text{H}^+) = 0.59 + 0.58 \chi(\text{HNC0})$	0.87
4	$\chi(^{13}\text{CS}) = 0.89 - 0.04 \chi(\text{HNC0})$	-0.25
5	$\chi(\text{C}_2\text{H}) = 0.19 + 0.09 \chi(\text{HNC0})$	0.81
6	$\chi(\text{H}^{13}\text{CO}^+) = 1.23 + 0.88 \chi(\text{HNC0})$	0.80
7	$\chi(\text{SiO}) = 0.38 + 0.22 \chi(\text{HNC0})$	0.49

iii) undetected and widespread lower mass protostars. In our ATLASGAL sample, SiO emission is mostly detected in clumps with signs of star formation (typically associated with 8 μm sources, 24 μm sources and/or extended 4.5 μm emissions). Outflows have also been detected in some sources (Yu & Wang 2014). The average SiO line width in the sample is $\sim 9 \text{ km s}^{-1}$, indicating the presence of outflow activity. Zinchenko et al. (2000) found the SiO integrated line intensities correlate well with those of thermal HNC0 emission in massive galactic dense cores, indicating a common production mechanism for these two species. Rodríguez-Fernández et al. (2010) tested this hypothesis by observing the L1157 molecular outflow. Their result indicates shocks actually enhance the HNC0 abundance in the star-forming regions of galactic nuclei. Moreover, Li et al. (2013) found

possible shock enhancement of HNC0 in Orion KL and W75OH. They regard collisional excitation as likely to be the dominant excitation mechanism for HNC0 emission. We also found the sizes of HNC0 clumps are comparable to those of SiO clumps. However, as shown in the bottom panel of Figure 20, our study indicates that the abundance of HNC0 does not correlate well with that of SiO. This may be because HNC0 and SiO trace different parts of shocked gas. Flower et al. (1995) regard gas-phase HNC0 as mainly enhanced by low-velocity shocks. Using interferometric data, Blake et al. (1996) found the spatial distributions of HNC0 and SiO emissions are quite different. The average HNC0 line width in the sample is $\sim 5 \text{ km s}^{-1}$, less than that of SiO.

Figure 21 plots the HNC0 velocity widths versus those of HN^{13}C and SiO. We can see that the veloc-

ity width of HNC0 tends to be wider than that of HN^{13}C (a tracer of unshocked dense and cold gas) but is narrower than that of SiO, indicating HNC0 traces relatively low-velocity shocks. Figure 22 shows the $\chi(\text{HNC0})/\chi(\text{SiO})$ relative abundance ratios plotted as a function of the line widths of HNC0 (the left panel) and SiO (the right panel). There is a hint that in the low-velocity shocks traced by HNC0, the HNC0 abundance increases faster than SiO. However, in the relatively high-velocity shocks traced by SiO, the SiO abundance increases faster than HNC0. UV radiation induced by high-velocity shocks (Viti et al. 2002) might destroy HNC0. In our sample, two clumps (AGAL331.709+00.582 and AGAL331.709+00.602) are known as “extended green objects” (EGOs) found by Cyganowski et al. (2008). EGOs are believed to be good candidates of MYSOs with outflows. In addition, these two clumps are found to be embedded in the same IRDC of MSXDC G331.71+00.59 (Yu & Wang 2013), indicating the same initial chemical conditions. However, we found that AGAL331.709+00.508 has relatively strong SiO emissions and weak HNC0 emissions, but the situations in AGAL331.709+00.602 are the opposite (see Figs. 8 and 9).

The left panel of Figure 23 shows the velocity-width (moment 2) map of SiO overlaid with HNC0 integrated intensity contours. It seems that even though these two clumps are located in the same IRDC, their physical conditions are quite different: the shocks traced by SiO in AGAL331.709+00.582 are much faster than those in AGAL331.709+00.602 (see the right panel of Fig. 23). Fast-velocity shocks may be destroying the molecule HNC0 in AGAL331.709+00.582. We expect high spatial resolution observations carried out in the future to study the differences of HNC0 and SiO in different parts of shocked gas.

5 SUMMARY

Using data from MALT90, we present a molecular line study of a sample of ATLASGAL clumps. By comparing with other molecular species, we found that the abundance of HNC0 correlates well with HC_3N , HNC, C_2H , H^{13}CO^+ and N_2H^+ . However, the correlations between $\chi(\text{HNC0})$ and species such as ^{13}CS and SiO are not so good. Previous studies indicate HNC0 and SiO are good tracers of interstellar shocks. However, in this study, we found the abundance of HNC0 does not correlate well with that of SiO. We suggest this may

be because HNC0 traces the low-velocity shocks while SiO traces relatively high-velocity shocks. We found that in the low-velocity shocks, the HNC0 abundance increases faster than that of SiO. But in the relatively high-velocity shocks traced by SiO, the SiO abundance increases faster than that of HNC0. We suggest that in the IRDC MSXDC G331.71+00.59, high-velocity shocks are destroying the molecule HNC0.

Acknowledgements We thank the referee for constructive comments that improved this paper. This paper has made use of information from the APEX Telescope Large Area Survey of the Galaxy. The ATLASGAL project is a collaboration between the Max-Planck-Gesellschaft, the European Southern Observatory (ESO) and the Universidad de Chile. This research made use of data products from the Millimetre Astronomy Legacy Team 90 GHz (MALT90) survey. The Mopra telescope is part of the Australia Telescope and is funded by the Commonwealth of Australia for operation as a National Facility managed by CSIRO. This paper is supported by the National Natural Science Foundation of China (Grant No. 11503037).

References

- Allen, M., & Robinson, G. W. 1977, *ApJ*, 212, 396
- Bergin, E. A., Ciardi, D. R., Lada, C. J., Alves, J., & Lada, E. A. 2001, *ApJ*, 557, 209
- Blake G. A., Mundy L. G., Carlstrom J. E., et al., 1996, *ApJ* 472, L49
- Brown, R. L. 1981, *ApJ*, 248, L119
- Chapman, J. F., Millar, T. J., Wardle, M., Burton, M. G., & Walsh, A. J. 2009, *MNRAS*, 394, 221
- Churchwell, E., Wood, D., Myers, P. C., & Myers, R. V. 1986, *ApJ*, 305, 405
- Contreras, Y., Schuller, F., Urquhart, J. S., et al. 2013, *A&A*, 549, A45
- Cyganowski, C. J., Whitney, B. A., Holden, E., et al. 2008, *AJ*, 136, 2391
- Flower, D. R., Pineau des Forets, G., & Walmsley, C. M. 1995, *A&A*, 294, 815
- Foster, J. B., Jackson, J. M., Barnes, P. J., et al. 2011, *ApJS*, 197, 25
- Foster, J. B., Rathborne, J. M., Sanhueza, P., et al. 2013, *PASA*, 30, e038
- Garrod, R. T., Wicicus Weaver, S. L., & Herbst, E. 2008, *ApJ*, 682, 283
- Guzmán, A. E., Sanhueza, P., Contreras, Y., et al. 2015, *ApJ*, 815, 130
- Hennemann, M., Birkmann, S. M., Krause, O., et al. 2009, *ApJ*, 693, 1379

- Iglesias, E. 1977, *ApJ*, 218, 697
- Jackson, J. M., Armstrong, J. T., & Barrett, A. H. 1984, *ApJ*, 280, 608
- Jackson, J. M., Rathborne, J. M., Foster, J. B., et al. 2013, *PASA*, 30, e057
- Jiménez-Serra, I., Caselli, P., Tan, J. C., et al. 2010, *MNRAS*, 406, 187
- Ladd, N., Purcell, C., Wong, T., & Robertson, S. 2005, *PASA*, 22, 62
- Li, J., Wang, J. Z., Gu, Q. S., & Zheng, X. W. 2013, *A&A*, 555, A18
- Liu, X. L., Xu, J. L., Ning, C. C., et al. 2018, *RAA (Research in Astronomy and Astrophysics)*, 18, 4
- Louvet, F., Motte, F., Gusdorf, A., et al. 2016, *A&A*, 595, A122
- Martín-Pintado, J., Bachiller, R., & Fuente, A. 1992, *A&A*, 254, 315
- Martín, S., Requena-Torres, M. A., Martín-Pintado, J., & Mauersberger, R. 2008, *ApJ*, 678, 245
- Meier, D. S., & Turner, J. L. 2005, *ApJ*, 618, 259
- Miettinen, O. 2014, *A&A*, 562, A3
- Müller, H. S. P., Schlöder, F., Stutzki, J., & Winnewisser, G. 2005, *Journal of Molecular Structure*, 742, 215
- Müller, H. S. P., Thorwirth, S., Roth, D. A., & Winnewisser, G. 2001, *A&A*, 370, L49
- Purcell, C. R., Balasubramanyam, R., Burton, M. G., et al. 2006, *MNRAS*, 367, 553
- Purcell, C. R., Longmore, S. N., Burton, M. G., et al. 2009, *MNRAS*, 394, 323
- Rathborne, J. M., Whitaker, J. S., Jackson, J. M., et al. 2016, *PASA*, 33, e030
- Rodríguez-Fernández, N. J., Tafalla, M., Gueth, F., & Bachiller, R. 2010, *A&A*, 516, A98
- Sanhueza, P., Jackson, J. M., Foster, J. B., et al. 2012, *ApJ*, 756, 60
- Schilke, P., Walmsley, C. M., Pineau des Forets, G., & Flower, D. R. 1997, *A&A*, 321, 293
- Schuller, F., Menten, K. M., Contreras, Y., et al. 2009, *A&A*, 504, 415
- Snyder, L. E., & Buhl, D. 1972, *ApJ*, 177, 619
- Sreenilayam, G., & Fich, M. 2011, *AJ*, 142, 4
- Tideswell, D. M., Fuller, G. A., Millar, T. J., & Markwick, A. J. 2010, *A&A*, 510, A85
- Tucker, K. D., Kutner, M. L., & Thaddeus, P. 1974, *ApJ*, 193, L115
- Turner, B. E., Terzieva, R., & Herbst, E. 1999, *ApJ*, 518, 699
- Velilla Prieto, L., Sánchez Contreras, C., Cernicharo, J., et al. 2015, *A&A*, 575, A84
- Viti, S., Natarajan, S., & Williams, D. A. 2002, *MNRAS*, 336, 797
- Yu, N.-P., & Wang, J.-J. 2013, *RAA (Research in Astronomy and Astrophysics)*, 13, 28
- Yu, N., & Wang, J.-J. 2014, *MNRAS*, 440, 1213
- Yu, N., & Xu, J. 2016, *ApJ*, 833, 248
- Zinchenko, I., Henkel, C., & Mao, R. Q. 2000, *A&A*, 361, 1079